Supplementary information

Spin Crossover or Intra-Molecular Electron Transfer in a Cyanido-Bridged Fe/Co Dinuclear Dumbbell: A Matter of State

Ie-Rang Jeon,[a,b,c,d] Sergiu Calancea,[c,d] Anangamohan Panja,[c,d] Dalice M. Piñero Cruz,[a,b] Evangelia S. Koumousi,[a,b,c,d] Pierre Dechambenoit,[a,b] Claude Coulon,[a,b] Alain Wattiaux,[c,d] Patrick Rosa,[c,d] Corine Mathonière,*[c,d] and Rodolphe Clérac*[a,b]

[a] *CNRS, CRPP, UPR 8641, Pessac, F-33600, France. Fax: +33 5 56 84 56 00; Tel: +33 5 56 84 56 50; E-mail: clerac@crpp-bordeaux.cnrs.fr*
[b] *Univ. Bordeaux, CRPP, UPR 8641, Pessac, F-33600, France.*
[c] *CNRS, UPR 9048, ICMCB, Pessac, F-33600, France. Fax: +33 5 40 00 26 49; Tel: +33 5 40 00 26 82; E-mail: mathon@icmcb-bordeaux.cnrs.fr*
[d] *Univ. Bordeaux, ICMCB, UPR 9048, Pessac, F-33600, France.*

Contents

Table S1 Crystallographic data of compounds **1** - **3**. **p. 2**

Table S2 Crystallographic data of **[FeCo]** at 370 K and 90 K. **p. 2**

Table S3 Selected bond lengths [Å] and angles [°] for **[FeCo]** and for **1** and **2**. **p. 3**

Figure S1 Portion of the crystal structure of **1**. **p. 3**

Figure S2 Portion of the crystal structure of **2**. **p. 4**

Figure S3 Portion of the crystal structure of **3**. **p. 4**

Figure S4 ORTEP-type view of the **[FeCo]** at 90 K. **p. 4**

Figure S5 Packing diagrams of **[FeCo]** in the *ac* plane. **p. 5**

Figure S6 Packing diagrams of **[FeCo]** in the *ab* plane. **p. 5**

Figure S7 Powder X-ray diffraction patterns of **[FeCo]** compared with the simulation obtained from the single crystal data. **p. 6**

Figure S8 Thermogravimetric analysis (TGA) of **[FeCo]**. **p. 6**

Figure S9 Temperature dependence of χT product for **[FeCo]** in DMSO. **p. 6**

Figure S10 UV-vis spectra of **1** and $\mathbf{1}^-$; **3** and $\mathbf{3}^-$; **[FeCo]** and $[\mathbf{FeCo}]^-$; $[\mathbf{H_2FeCo}]^{2+}$ and $[\mathbf{H_2FeCo}]^+$ at 298 K. **p. 7**

Figure S11 ^{1}H NMR spectra of **1**, **2**, **3** and **[FeCo]** in *d*-DMSO. **p. 8**

Figure S12 ^{1}H-^{1}H COSY spectrum of **2** in *d*-DMSO. **p. 10**

Figure S13 ^{1}H-^{1}H COSY spectrum of **[FeCo]** in *d*-DMSO. **p. 10**

Figure S14 ^{1}H NMR spectrum of **[FeCo]** in *d*-DMSO with 10 eq. of *d*-TFA. **p. 11**

Figure S15 ^{1}H-^{1}H COSY spectrum of **[FeCo]** in *d*-DMSO with 10 eq. of *d*-TFA. **p. 11**

Figure S16 Cyclic voltammograms of **1** in DMSO and **2** in CH_3CN. **p. 12**

Figure S17 Cyclic voltammograms of **1** and **3** in DMSO. **p. 12**

Theoretical Analysis of UV-vis spectra. **p. 13**

Figure S18 UV-vis spectroscopic characterization of **[FeCo]** solution upon the addition of trifluoromethanesulfonic acid (TfOH). **p. 17**

Figure S19 Evolution of the UV-vis spectra upon TFA addition to a DMSO solution of **1**. **p. 18**

Table S1 | Crystallographic data of compounds **1 - 3.**

	1	**2**	**3**
Empirical formula	$C_{54}H_{95}FeN_{10}O_6$	$C_{29}H_{27}B_2CoF_8N_5O$	$C_{22}H_{15}FeN_8O$
Formula weight, g.mol^{-1}	1036.25	694.11	463.27
Crystal system	Monoclinic	Monoclinic	Monoclinic
Space group	$P2_1$	$C2/c$	$P2_1/c$
Wavelength, Å	0.71073	0.71073	0.71073
Temperature, K	100	120	100
a, Å	21.267(2)	21.346(5)	10.9398(12)
b, Å	11.483(13)	12.362(5)	22.107(3)
c, Å	26.049(3)	12.855(4)	16.8809(19)
β, ^{o}	111.875(2)	120.033(13)	92.003(6)
V, Å^3	5903.4(11)	2936.5(17)	4080.1(8)
Z	4	4	8
ρ_{calcd}, Mg m^{-3}	1.166	1.570	1.508
μ, mm^{-1}	0.309	0.670	0.773
Refections coll./unique	39068 / 20672	19792 / 4285	84823 / 7485
R(int)	0.0375	0.0368	0.1045
[a]R_1 ($I>2\sigma(I)$)	0.0846	0.0314	0.0513
[b]wR_2 (all)	0.2525	0.0842	0.1563
GoF	1.028	1.058	1.020

[a]$R_1 = \Sigma||F_0| - |F_C||/\Sigma|F_0|$, and [b]$wR_2 = [\Sigma w(F_0^2 - F_C^2)^2/\Sigma w(F_o^2)^2]^{1/2}$

Table S2 | Crystallographic data of compound **[FeCo]** at 370 K and 90 K.

	370 K	**90 K**
Empirical formula	$C_{107}H_{92}Co_2Fe_2N_{26}O_5$	$C_{107}H_{92}Co_2Fe_2N_{26}O_5$
Formula weight, g mol^{-1}	2051.63	2051.63
Crystal system	Monoclinic	Monoclinic
Space group	$P2_1/c$	$P2_1/c$
Wavelength, Å	0.71073	0.71073
a, Å	13.655(2)	13.560(1)
b, Å	14.348(2)	14.209(1)
c, Å	25.328(3)	24.965(2)
β, ^{o}	102.313(5)	103.148(3)
V, Å^3	4747.9(10)	4697.7(6)
Z	2	2
ρ_{calcd}, Mg m^{-3}	1.405	1.450
μ, mm^{-1}	0.700	0.722
Refections coll./unique	43392/8774	33940/8376
R(int)	0.0269	0.0358
[a]R_1 ($I>2\sigma(I)$)	0.0511	0.0500
[b]wR_2 (all)	0.1356	0.1364
GoF[a]	1.103	1.125

[a]$R_1 = \Sigma||F_0| - |F_C||/\Sigma|F_0|$, and [b]$wR_2 = [\Sigma w(F_0^2 - F_C^2)^2/\Sigma w(F_0^2)^2]^{1/2}$

Table S3 | Selected bond lengths [Å] and angles [°] for **[FeCo]** at 90 and 370 K, and for **1** and **2**.

	370 K	**90 K**		**1**	**2**
average (Co-N)	2.108(3)	2.058(3)	average (Co-N)		2.116(2)
average (Fe-N)	1.938(3)	1.934(3)	average (Fe-N)	1.947(6)	
average (Fe-C)	1.943(4)	1.948(4)	average (Fe-C)	1.954(7)	
Co1-N1	2.191(2)	2.242(3)	Co1-N1		2.141(1)
Co1-N2	2.182(3)	2.228(3)	Co1-N2		2.133(2)
Co1-N3	2.100(3)	1.999(3)	Co1-N3		2.093(2)
Co1-N4	2.106(3)	2.001(3)			
Co1-N5	2.062(2)	1.958(3)			
Co1-N6	2.009(3)	1.923(3)	Co1-O1		2.057(2)
Fe1-N7	1.946(3)	1.945(3)	Fe1-N1	1.934(6)	
			Fe2-N6	1.947(5)	
Fe1-N9	1.936(3)	1.928(3)	Fe1-N2	1.954(6)	
			Fe2-N7	1.961(7)	
Fe1-N10	1.932(3)	1.929(3)	Fe1-N3	1.938(5)	
			Fe2-N8	1.945(8)	
Fe1-C30	1.892(3)	1.890(4)	Fe1-C20	1.962(8)	
			Fe2-C42	1.963(7)	
Fe1-C31	1.972(4)	1.978(4)	Fe1-C21	1.974(9)	
			Fe2-C43	1.971(7)	
Fe1-C32	1.966(4)	1.977(4)	Fe1-C22	1.95(1)	
			Fe2-C44	1.903(7)	
Co1-N6-C30	168.2(3)	172.0(3)	N13-C20-Fe1	179.4(8)	
N6-C30-Fe1	178.0(3)	177.1(3)	N15-C44-Fe2	177.4(8)	

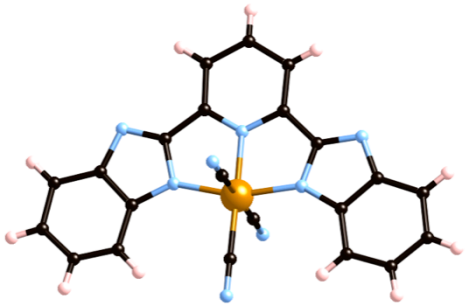

Figure S1 | Portion of the crystal structure of **1** at 100 K. Yellow, Fe; sky blue, N; black, C; pink, H. Counter ions and lattice solvents are omitted for clarity.

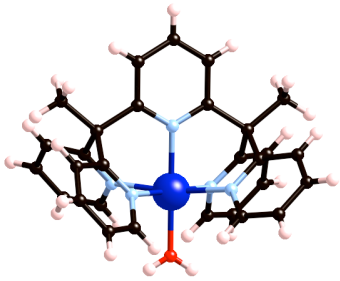

Figure S2 | Portion of the crystal structure of **2** at 120 K. Blue, Co; sky blue, N; black, C; pink, H. Counter ions are omitted.

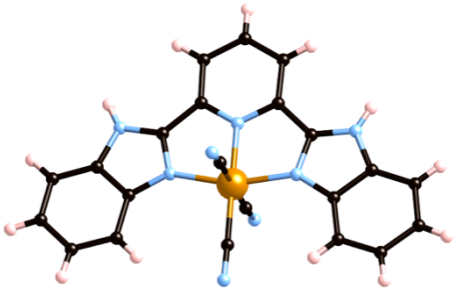

Figure S3 | Portion of the crystal structure of **3** at 100 K. Yellow, Fe; sky blue, N; black, C; pink, H. Lattice solvents are omitted for clarity.

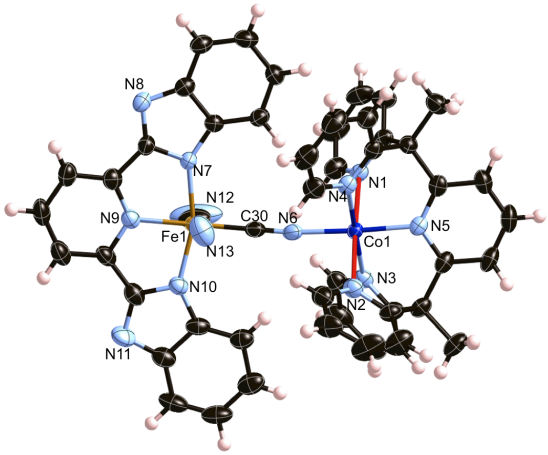

Figure S4 | ORTEP-type view of **[FeCo]** at 90 K with thermal ellipsoids at 50 % probability level. The Jahn-Teller elongation axis at low temperature is highlighted in red. Yellow, Fe; blue, Co; sky blue, N; black, C; pink, H. Lattice solvents are omitted for clarity.

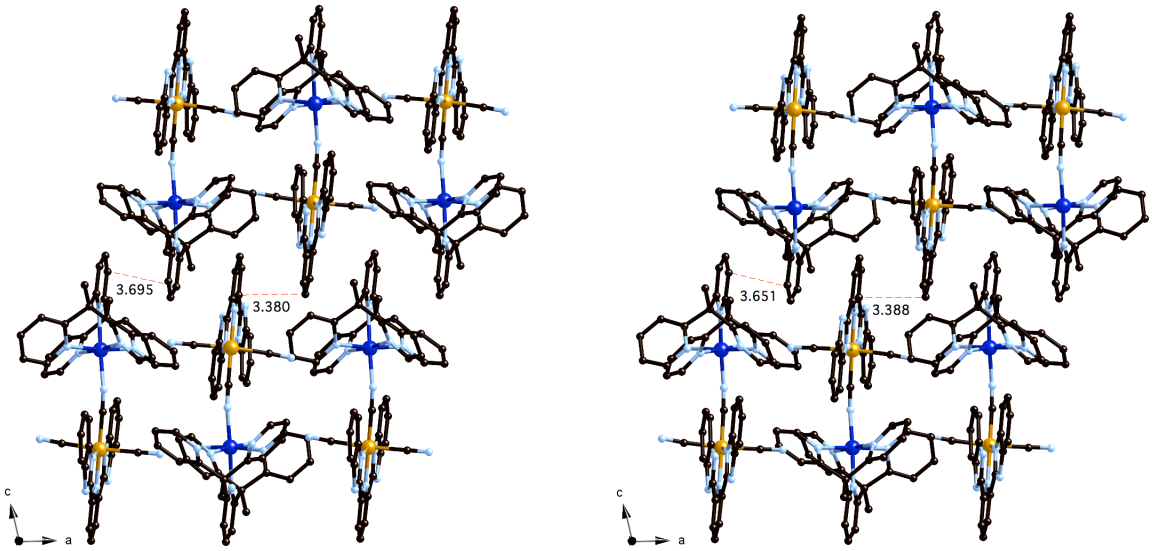

Figure S5 | Packing diagram of **[FeCo]** in the *ac* plane illustrating intercomplex π–π interactions between $PY5Me_2$ ligands and adjacent BBP ligands, for data collected at 370 K (left) and 90 K (right). Lattice solvent molecules and hydrogen atoms are omitted for clarity.

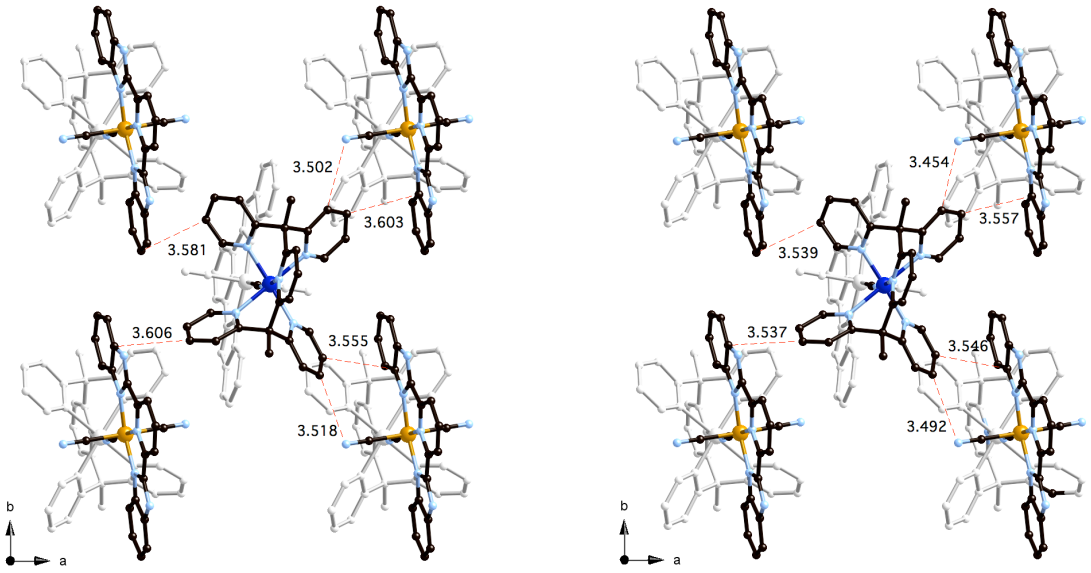

Figure S6 | Packing diagram of **[FeCo]** in the *ab* plane illustrating intercomplex short contacts between $PY5Me_2$ ligands and neighbouring BBP/cyanido ligands, for data collected at 370 K (left) and 90 K (right). Ligands associated in the further layer along the crystallographic *c* direction are shown in grey. Lattice solvent molecules and hydrogen atoms are omitted for clarity.

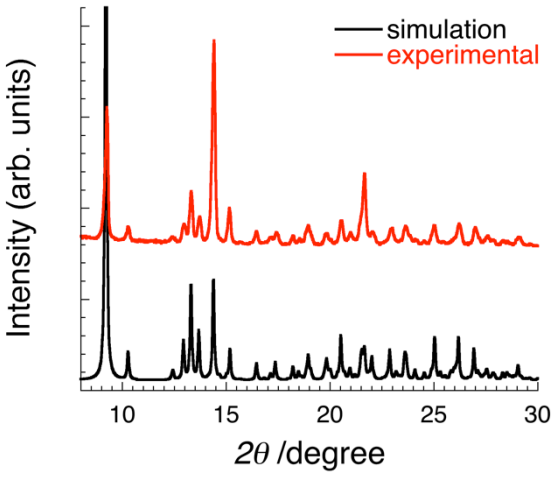

Figure S7 | Powder X-ray diffraction patterns of **[FeCo]** (red, at 298 K) compared with the simulation (black) obtained from single crystal data collected at 270 K.

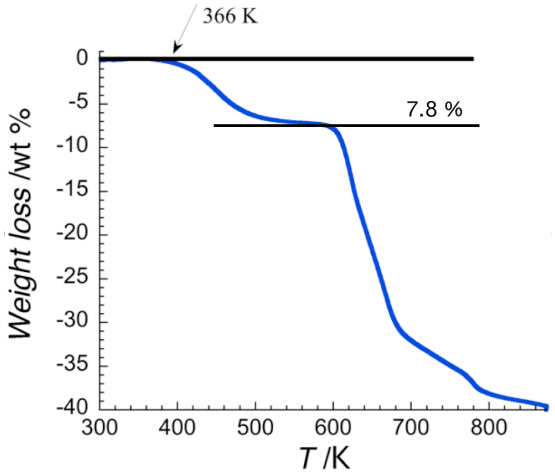

Figure S8 | Thermogravimetric trace of **[FeCo]** at 5 K/min. Weight loss corresponding to 2.5 MeOH molecules is 7.8%.

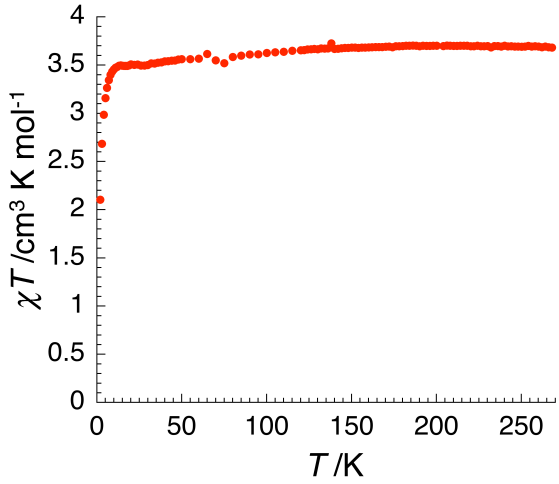

Figure S9 | Temperature dependence of χT product for **[FeCo]** in DMSO (3.05×10^{-5} M). Data are collected at an applied field of 10000 Oe.

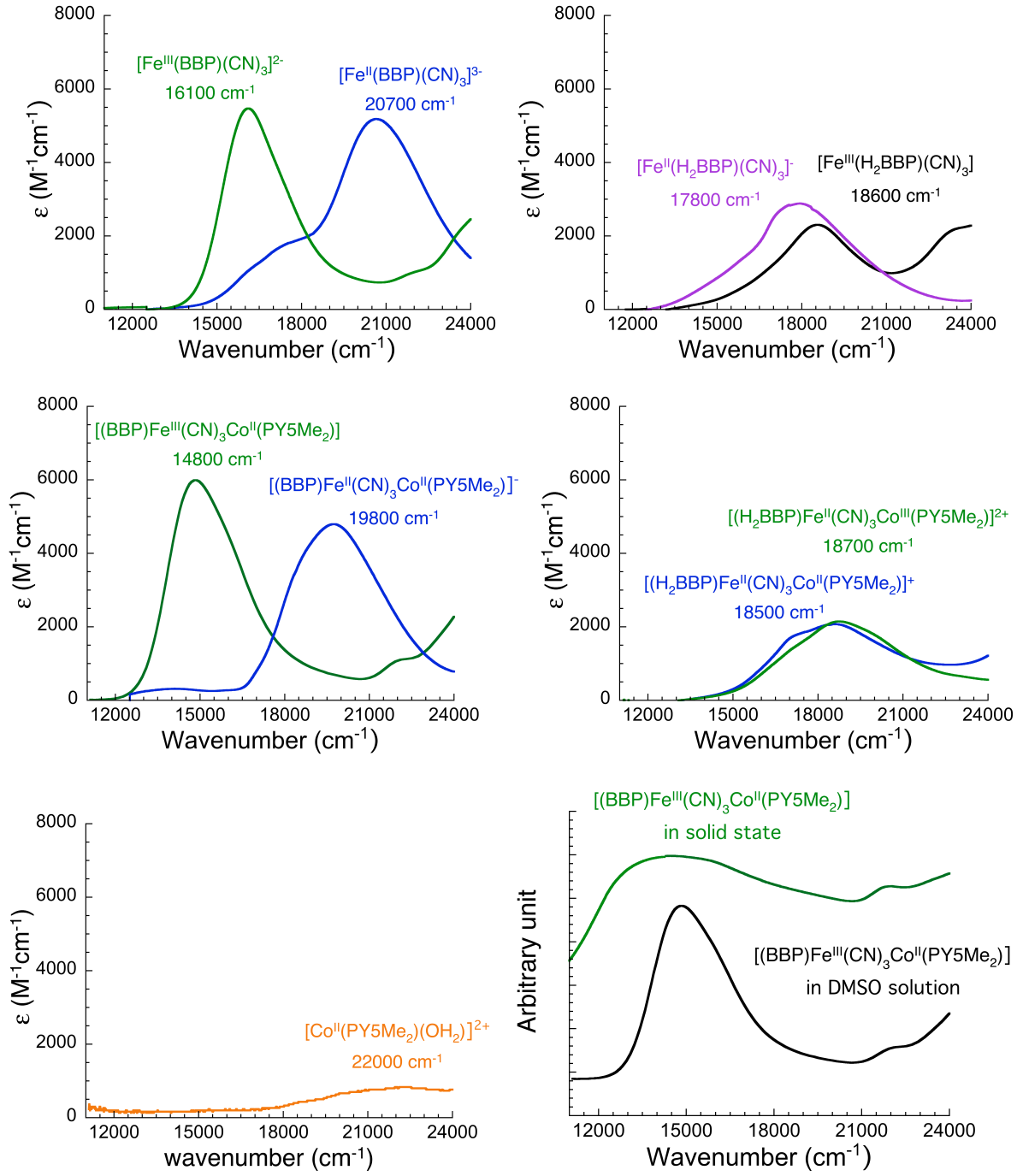

Figure S10 | UV-vis spectra at 298 K of (left, top) **1** and its reduced analogue **1**$^{-}$ (obtained at a -1.9 V stable potential) with a concentration of 4.8 mM in DMSO; (right, top) diprotonated form of **1** (obtained *in situ* after direct treatment with 4 eq. of *d*-TFA; i.e. complex **3**) and its reduced species (obtained at a -1 V stable potential) with a concentration of 4.2 mM in DMSO; (middle left) **[FeCo]** and **[FeCo]**$^{-}$ (obtained at a -1.4 V stable potential) with a concentration of 4.8 mM in DMSO; and (middle right) **[H$_2$FeCo]**$^{2+}$ and **[H$_2$FeCo]**$^{+}$ (obtained at a -1.5 V stable potential; **[H$_2$FeCo]**$^{2+}$ has been obtained *in situ* after direct treatment with 4 eq. of *d*-TFA) with a concentration of 4.2 mM in DMSO; (bottom left) **2** with a concentration of 0.27 mM in DMSO; (bottom right) **[FeCo]** in solid state compared to the **[FeCo]** spectrum in DMSO solution (with a concentration of 4.8 mM).

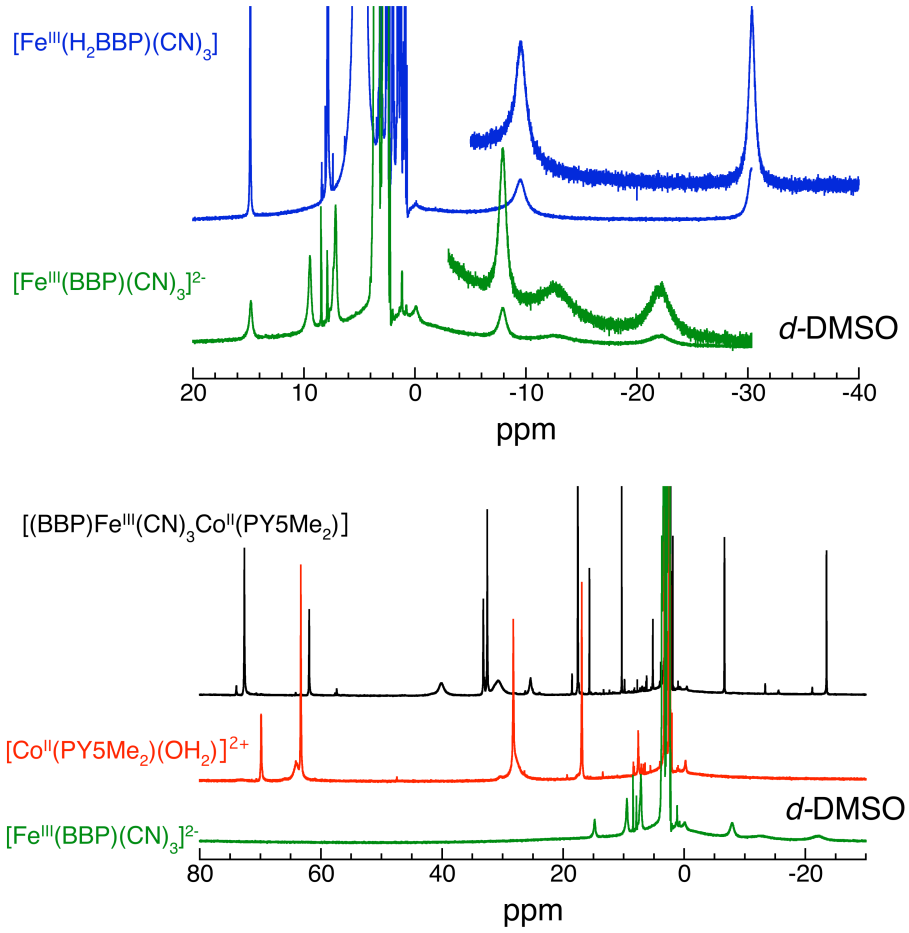

Figure S11 | ^{1}H NMR spectra in *d*-DMSO at 298 K of (top) **1** and its diprotonated analogue (obtained *in situ* after treatment with 10 eq. of *d*-TFA; i.e. complex **3**) emphasizing their paramagnetic nature and thus a +III oxidation state of the Fe ions; and (bottom) **1**, **2** and **[FeCo]** emphasizing the absence of dissociation of the paramagnetic **[FeCo]** pair in solution as the Fe and Co precursor NMR signatures are clearly absent on the NMR spectrum of **[FeCo]**. It is worth mentioning that due to weak and broad NMR signals (paramagnetic) for **1**, the ^{1}H-^{1}H COSY measurements were not informative and are thus not shown.

Comment on the NMR data: It is worth mentioning that when the **[FeCo]** complex is solubilized in DMSO, weak interactions (H-bonding, π stacking…) between hypothetically separated mononuclear ionic precursors, $[Fe^{III}(BBP)(CN)_3]^{2-}$ and $[Co^{II}(PY5Me_2)(DMSO)]^{2+}$, could also lead to some NMR shifts. Nevertheless, the two ionic complexes do not offer the possibility of H-bonding between them and only H-bonding between the Fe precursors might be possible. In this latter case, the NMR spectra of the Co building block would not be affected as it is indeed observed experimentally. Moreover, π stacking is almost never observed in diluted solutions especially in strongly polar solvents like DMSO (that also prevents any intermolecular H-bonding). Therefore only the cyanide coordination to the Co(II) ion can explain the observed NMR shift compared to the original building blocks.

If any dissociation of the **[FeCo]** complex would be present in solution, the high dipolar moment of DMSO will insure the ionic partners to be well-separated. With usual NMR concentrations (≈ 10 mg

for 0.5 mL) the expected separations between the two moieties of the dissociated **[FeCo]** complex would be on the order of 44 Å. Indeed this separation is incompatible with the qualitative analysis of the NMR shift and thus only a CN coordination on the Co(II) can explained the observed NMR results that are also further supported by CV and UV-vis measurements (Figs 4, 6, S10 and S16-S19).

Considering the equations for the hyperfine shift (I. Bertini, C. Luchinot, G. Parigi, *Solution NMR of Paramagnetic Molecules. Current Methods in Inorganic Chemistry*, **2001**, *2*, Elsevier), the following relation has been established:

$$\delta_{pc} = \frac{1}{12\pi r^3}\left(\chi_{//} - \chi_{\perp}\right)\left(3\cos^2\theta - 1\right)$$

where δ_{pc} is the pseudo-contact shift, expressed in ppm, r and θ are distance and angle between the resonating nucleus and the spin density center (in the transition metal approximation), χ are the anisotropic susceptibilities in the axial approximation, expressed in SI units (m^3). Here both $[Fe^{III}(BBP)(CN)_3]^{2-}$ and $[Co^{II}(PY5Me_2)(DMSO)]^{2+}$ species are anisotropic paramagnetic centers, which can cause hyperfine shifts by dipolar interactions for the protons of a given entity. The order of magnitude of the NMR shift can be roughly estimated in the case of the **[FeCo]** dissociation into its ionic constituents. For that, it is necessary to consider only the Co^{II} center that is more anisotropic and has a higher spin state than the low spin Fe^{III} ion. The orbital contribution and the zero-field splitting can also be neglected since the NMR spectra are measured at room temperature. Considering for example g values for high-spin $Co^{II}N_6$ complexes (see for example $[Co(HC(pz)_3)_2](NO_3)_2$ and $[Co(HB(pz)_3)_2]$ in A. Bencini, D. Gatteschi, *ESR spectra of Metal Complexes of the First Transition Series in Low-Symmetry Environments*, in *Transition Metal Chemistry*, **1982**, *8*, G. A. Nelson, B. N. Figgis, Eds, Marcel Dekker, NY) as $g_{||} = 8$ and $g_{\perp} = 0.8$, this gives in SI units at 293 K:

$$\chi_{//} - \chi_{\perp} = 210.10^{-32}\ \mathrm{m}^3$$

For distances of about 44 Å between ions, absolute hyperfine NMR shift should be less than 1 ppm. The variations observed in the above ^1H NMR spectrum of the **[FeCo]** complex respective to the spectra of the isolated precursors support without ambiguity a much shorter interaction on the order of less than 10 Å. This short distance in a solvent with a high dipolar moment such as DMSO is not reasonable unless the complex retained its structural dinuclear integrity.

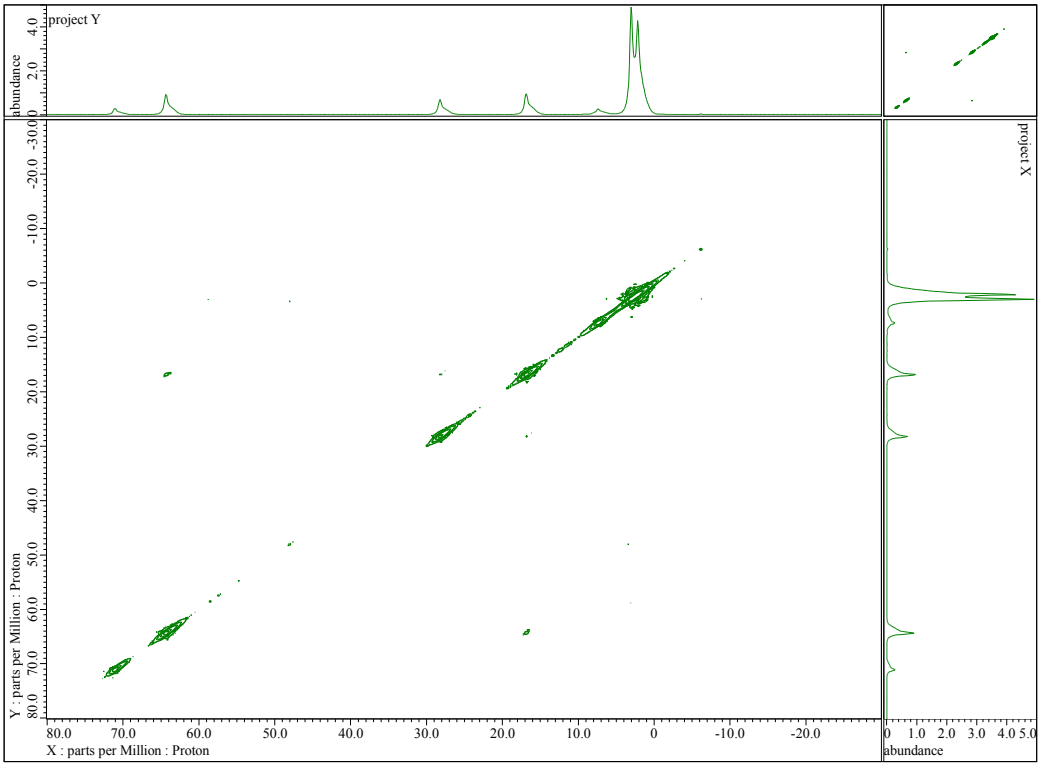

Figure S12 | ^{1}H-^{1}H COSY spectrum of **2** in *d*-DMSO at 298 K.

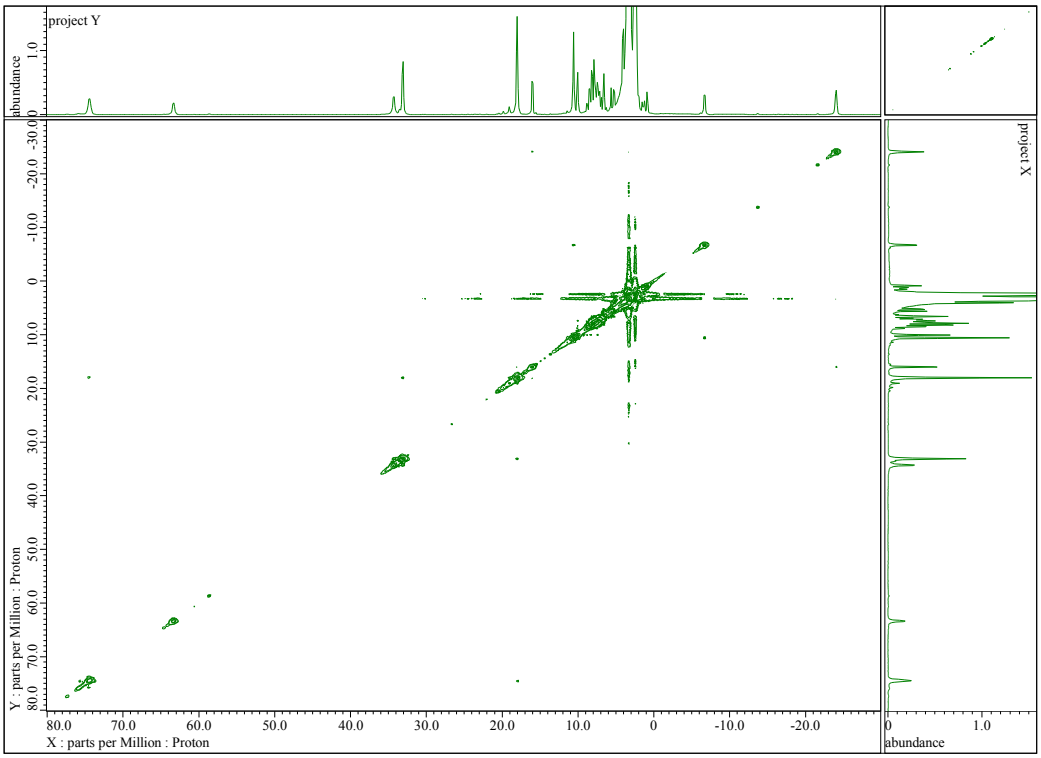

Figure S13 | ^{1}H-^{1}H COSY spectrum of **[FeCo]** in *d*-DMSO at 298 K.

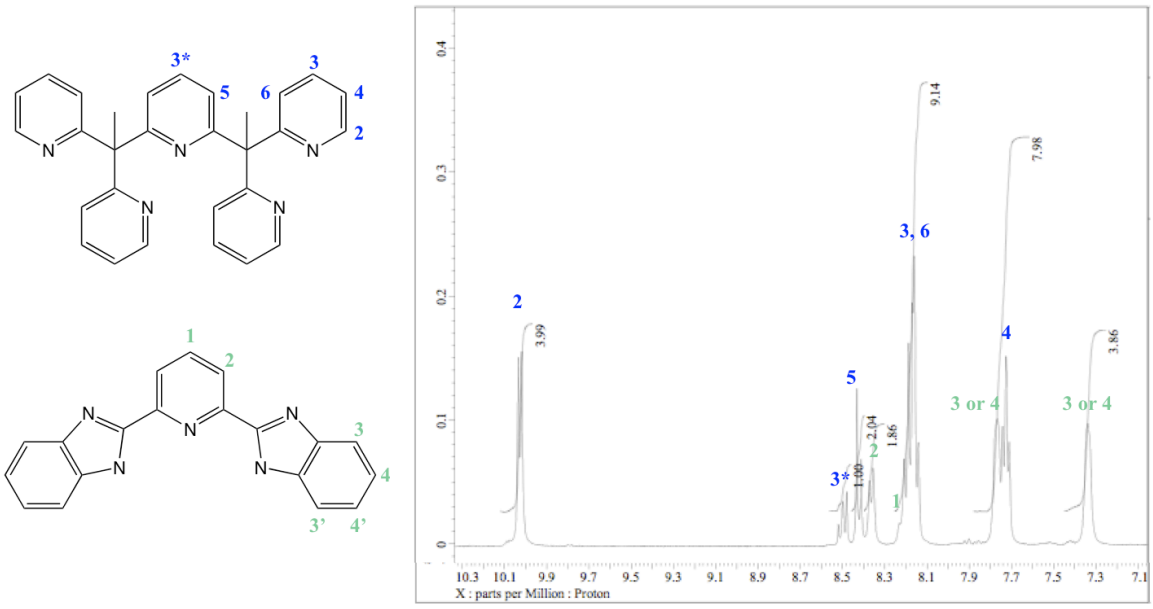

Figure S14 | ^{1}H NMR spectrum of **[FeCo]** in *d*-DMSO at 298 K after treatment with 10 eq. of *d*-TFA. The resonance peaks are attributed to each ^{1}H of the ligands.

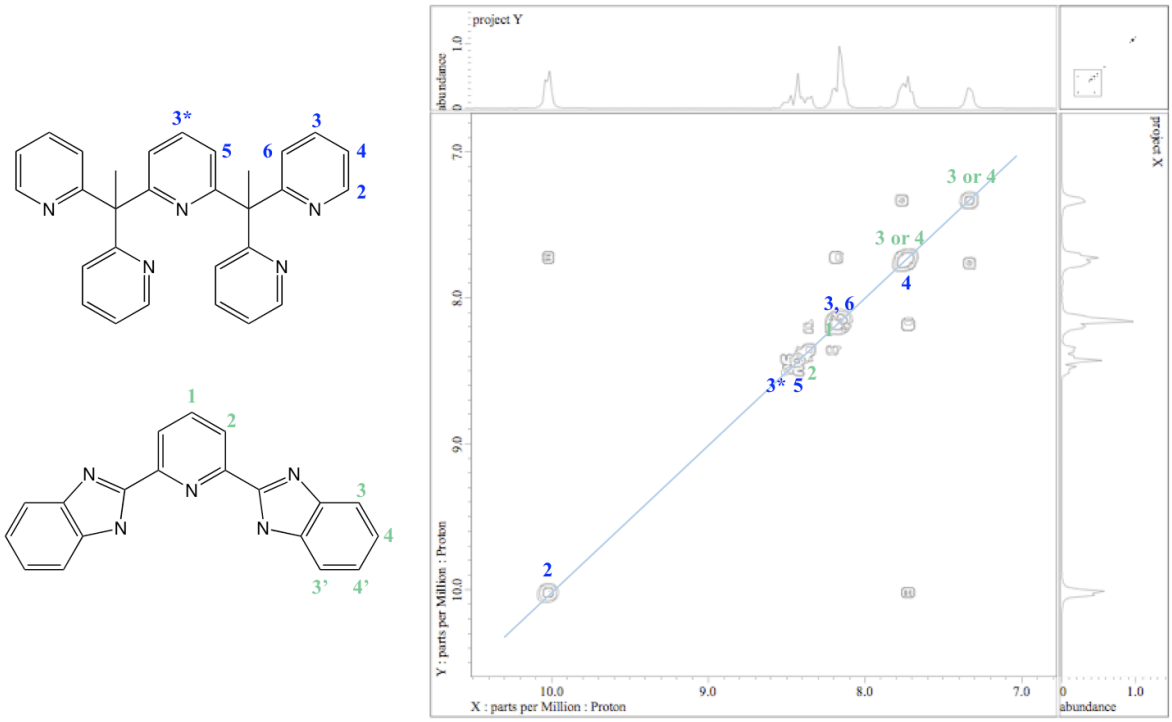

Figure S15 | ^{1}H-^{1}H COSY spectrum of **[FeCo]** in *d*-DMSO at 298 K after treatment with 10 eq. of *d*-TFA. The resonance peaks are attributed to each ^{1}H of the ligands.

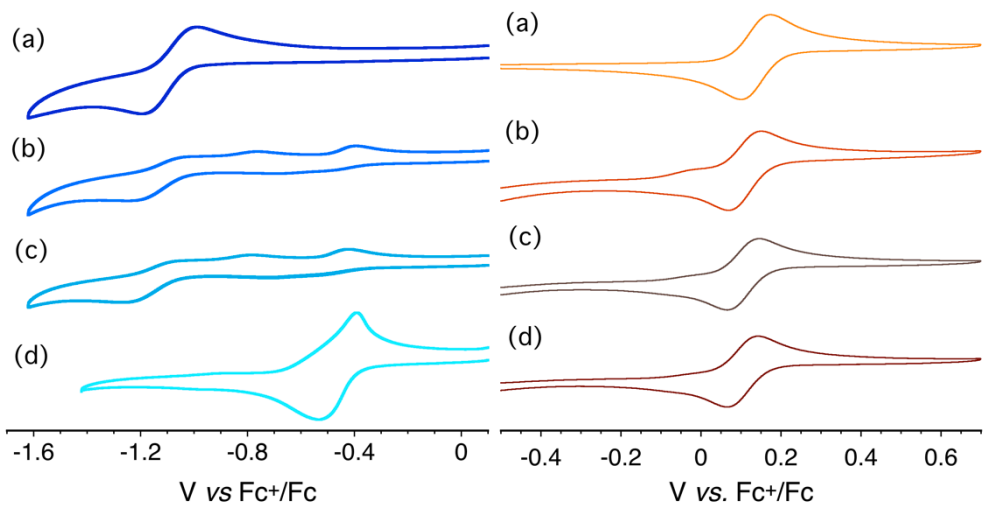

Figure S16 | Cyclic voltammograms of **1** in DMSO (left) and **2** in CH_3CN (right) at ≈ 1 mM. Potentials were referenced to the $[Cp_2Fe]^{1+/0}$ couple. As prepared (a); after 1 eq. of a TFA (b); after 2 eq. of a TFA (c); and after 3 eq. of TFA (d).

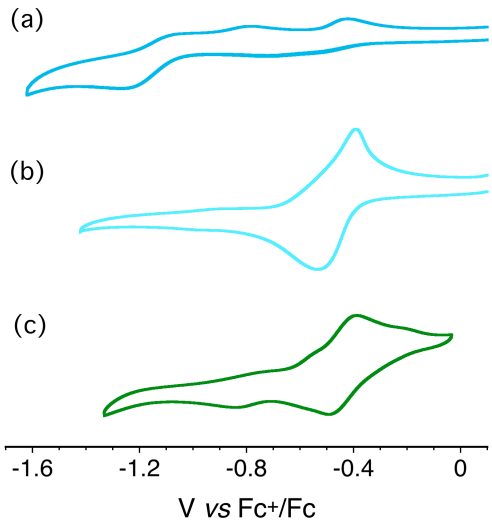

Figure S17 | Cyclic voltammograms of **1** and **3** in DMSO at ≈ 1 mM. Potentials were referenced to the $[Cp_2Fe]^{1+/0}$ couple. After 2 eq. of a TFA to **1** (a); after 3 eq. of a TFA to **1** (b); as prepared solution of **3** (c).

Theoretical analysis of UV-vis spectra

Given the fact that the protonation occurs on two nitrogen atoms of the BBP ligand for Fe building block as seen in **3**, we assume that the protonation on the dinuclear **[FeCo]** complex upon the acid addition also occurs on these two sites. Thus, the possible species in the solution can be non-protonated **[FeCo]** (= *D*), mono-protonated $\mathbf{[HFeCo]^+}$ (= HD^+), and di-protonated $\mathbf{[H_2FeCo]^{2+}}$ (= H_2D^{2+}) complexes, and we know that the latter one corresponds to the diamagnetic $\{Fe^{II}_{LS}\text{-CN-}Co^{III}_{LS}\}$ species. The reaction scheme is described as acid-base titration with the acidity of added acid (*HA*) given as K_a. The di-protonated species H_2D^{2+} is considered as diprotic acid with K_{a1} and K_{a2}.

As seen in Fig. 4, we can remark that the UV-vis spectra around 18700 cm^{-1} were hardly modified before the first equivalence point (< 1eq.). It suggests the quasi-absence of di-protonated H_2D^{2+} species and thus at a first approximation that all added protons produce mono-protonated HD^+ species. Then, the absorption around 14800 cm^{-1} is the signature of both mono-protonated HD^+ and non-protonated *D* species. The linear variation of the green curve in Fig. 4b confirms also the absence of H_2D^{2+} before 1 eq. of acid and furthermore, its slope of -0.5 indicates that the absorbance of the mono-protonated HD^+ species is twice weaker than the non-protonated *D* species (the observed slope would be 0 if the two species had the same absorbance intensity). From this, we can suppose that $K_{a1} \gg K_{a2}$ ($K_{a1} < 1$ and $K_{a2} \ll 1$). This is also true for the experiment with strong acid (see below and Fig. S18).

Protonation with a strong acid. In order to simplify the calculations, we first considered the protonation of *D* with a strong acid, for which the added acids are completely dissociated to generate protons. Therefore, we can define $[H^+]_0 = C_A$ (initial acid concentration) and $[D]_0 = C_0$ (initial concentration of *D*). Then the equilibriums involving H_2D^{2+} and HD^+ are described as:

$$H_2D^{2+} \rightleftharpoons HD^+ + H^+ \qquad K_{a1} \qquad (1)$$

$$HD^+ \rightleftharpoons D + H^+ \qquad K_{a2} \qquad (2)$$

Since $K_{a1} \gg K_{a2}$, the predominant reaction is the reverse reaction of (2): $D + H^+ \longrightarrow HD^+$. After this reaction, the new initial state is: $[H^+]_0 = 0$, $[D]_0 = C_0 - C_A$, $[HD^+]_0 = C_A$. Then until the first equivalence point ($C_A \leq C_0$), the predominant equilibrium is given by equation (3) ($x = [H_2D^{2+}]$):

$$2HD^+ \rightleftharpoons D + H_2D^{2+} \qquad K \qquad (3)$$

$$K = \frac{x(C_0 - C_A + x)}{(C_A - 2x)^2} = \frac{K_{a2}}{K_{a1}}$$

Considering K_{a2}/K_{a1} « 1, we obtain the following normalized concentration of each species ($r = C_A/C_0$):

$$\frac{[H_2D^{2+}]}{C_0} = -0.5 + 0.5r + 0.5\sqrt{(1-r)^2 + 8rK - 4r^2K} \quad (4)$$

$$\frac{[HD^{+}]}{C_0} = 1 - \sqrt{(1-r)^2 + 8rK - 4r^2K} \quad (5)$$

$$\frac{[D]}{C_0} = 0.5 - 0.5r + 0.5\sqrt{(1-r)^2 + 8rK - 4r^2K} \quad (6)$$

And at the first equivalence point ($C_A = C_0$):

$$\frac{[H_2D^{2+}]}{C_0} = \sqrt{K} \quad (7)$$

After the first equivalence point ($C_A > C_0$), the predominant reaction is then the reverse reaction of (1): $HD^+ + H^+ \longrightarrow H_2D^{2+}$ and thus the new initial state is:

(i) when $C_0 < C_A < 2C_0$, $[H^+]_0 = 0$, $[HD^+]_0 = 2C_0 - C_A$, $[D]_0 = 0$, $[H_2D^{2+}]_0 = C_A - C_0$

(ii) when $C_A > 2C_0$, $[H^+]_0 = C_A - 2C_0$, $[HD^+]_0 = 0$, $[D]_0 = 0$, $[H_2D^{2+}]_0 = C_0$

(iii) when $C_A = 2C_0$, $[H^+]_0 = 0$, $[HD^+]_0 = 0$, $[D]_0 = 0$, $[H_2D^{2+}]_0 = C_0$.

At the second equivalence point ($C_A = 2C_0$), the possible reaction is (1) (dissociation of the H_2D^{2+} in HD^+ and H^+) and thus:

$$\frac{K_{a1}}{C_0} = \frac{\alpha^2}{1-\alpha} = q \quad (8)$$

with $[H_2D^{2+}] = C_0(1-\alpha)$. If we make the reasonable approximation that reaction of (1) is the only possible one also for the $C_0 < C_A < 2C_0$ and $C_A > 2C_0$ regimes, then, the equilibrium constants can be written as below:

$$K_{a1} = \frac{[H^+](2C_0 - C_A + [H^+])}{C_A - C_0 - [H^+]} \qquad \text{for } C_0 < C_A < 2C_0 \quad (9)$$

$$K_{a1} = \frac{[HD^+](C_A - 2C_0 + [HD^+])}{C_0 - [HD^+]} \qquad \text{for } C_A > 2C_0 \quad (10)$$

Both equations give identical solutions for $[H_2D^{2+}]/C_0$ and $[HD^+]/C_0$ (with $q = K_{a1}/C_0$, $r = C_A/C_0$):

$$\frac{[H_2D^{2+}]}{C_0} = 0.5r + 0.5q - \sqrt{(1-0.5r)^2 + 0.5rq + 0.25q^2} \quad (11)$$

$$\frac{[HD^+]}{C_0} = 1 - 0.5r - 0.5q + \sqrt{(1-0.5r)^2 + 0.5rq + 0.25q^2} \qquad (12)$$

Protonation with a weak acid. When the pK_a of the added acid (HA) is close to the pK_{a1} of H_2D^{2+}, the following equilibriums of H_2D^{2+} and HD^+ should be considered:

$$H_2D^{2+} + A^- \rightleftharpoons HD^+ + HA \qquad K_{a1}/K_a \qquad (13)$$

$$HD^+ + A^- \rightleftharpoons D + HA \qquad K_{a2}/K_a \qquad (14)$$

with $[HA]_0 = C_A$ (initial acid concentration) and $[D]_0 = C_0$ (initial concentration of D). After the predominant reaction that is the reverse reaction of (14) ($D + HA \longrightarrow HD^+ + A^-$), the new initial state is: $[HA]_0 = 0$, $[D]_0 = C_0 - C_A$, $[HD^+]_0 = [A^-]_0 = C_A$. Therefore, before the first equivalence point ($C_A \le C_0$), the reaction (3) (K_{a2}/K_{a1}) and the reverse reaction of (14) (K_{a2}/K_a) are in competition and thus it is not possible to establish simple analytical expressions of $[D]$ and $[D^+]$.

After the first equivalence point ($C_A > C_0$), the predominant reaction is the reverse of (13) ($HD^+ + HA \longrightarrow H_2D^{2+} + A^-$) and the new initial state is:

(i) when $C_0 < C_A < 2C_0$, $[HA]_0 = 0$, $[HD^+]_0 = 2C_0 - C_A$, $[D]_0 = 0$, $[H_2D^{2+}]_0 = C_A - C_0$, $[A^-]_0 = C_A$

(ii) when $C_A > 2C_0$, $[HA]_0 = C_A - 2C_0$, $[HD^+]_0 = 0$, $[D]_0 = 0$, $[H_2D^{2+}]_0 = C_0$, $[A^-]_0 = 2C_0$

(iii) when $C_A = 2C_0$, $[HA]_0 = 0$, $[HD^+]_0 = 0$, $[D]_0 = 0$, $[H_2D^{2+}]_0 = C_0$, $[A^-]_0 = 2C_0$.

At the second equivalence point ($C_A = 2C_0$), the existing two reactants, H_2D^{2+} and A^-, can make (1) and (13) as the possible reactions and thus with $[H^+] = \beta C_0$:

$$\frac{K_{a1}}{C_0} = \frac{\beta^2(1 + 2C_0/K_a)}{1 - \beta(1 + 2C_0/K_a)} \qquad (15)$$

For both $C_0 < C_A < 2C_0$ and $C_A > 2C_0$ regimes, the solutions for $[H_2D^{2+}]/C_0$ and $[HD^+]/C_0$ are identical (with $q = K_{a1}/C_0$, $p = K_a/C_0$):

$$\frac{[H_2D^{2+}]}{C_0} = \frac{pr}{p+\beta} - 1 - \beta \qquad (16)$$

$$\frac{[HD^+]}{C_0} = -\frac{pr}{p+\beta} + 2 + \beta \qquad (17)$$

$$\left(\text{with } r = \frac{C_A}{C_0} = \beta\left(1 + \frac{\beta}{p}\right) + \left(\frac{q + 2\beta}{q + \beta}\right)\left(1 + \frac{\beta}{p}\right) \right)$$

In order to make an analysis with the foregoing developed model, we have conducted additional UV/vis absorption measurements upon addition of a strong acid, trifluoromethanesulfonic

acid (TfOH). TfOH was added to **[FeCo]** in DMSO at a regular interval, in order to see the protonation dependence of the absorbance band intensity (see Fig. S18). As seen for the experimental data with TFA before the first equivalence (see Fig. 4b), a straight line with a slope of -0.5 compares perfectly with the normalized absorbance at 14800 cm^{-1} before 1 eq. of TfOH addition ($C_A < C_0$) (see Fig. S18, bottom). This result confirms that the experimental green points in Fig. S18 (intensity of the absorption band at 14800 cm^{-1}) are only influenced by *D* and HD^+ species. On the basis of the -0.5 slope, it is straightforward to conclude that the absorbance of HD^+ is twice weaker than the one of *D*. Meanwhile, the absorption band at 18700 cm^{-1} can be attributed to H_2D^{2+}. Experimentally, a little increase of the normalized absorbance around 18700 cm^{-1} below 1 eq. was observed (see Figs. 4b and S18), which can be explained by a reaction, where two HD^+ dissociate into a *D* and a H_2D^{2+} complex (equation (3)). Then, the deduced normalized concentrations of HD^+, and H_2D^{2+} depending on $[H^+]$ (equations (11) & (12)) were compared with the experimental data above 1 eq. of TfOH addition ($C_A > C_0$) (see Fig. S18, bottom). A remarkable agreement is found between the experimental curves (green and purple) and the theoretical $[HD^+]/C_0$ and $[H_2D^{2+}]/C_0$ expressions. The best simulation of the experimental results is obtained with $K_{a1} = 6.7 \times 10^{-5}$ M^{-1} and $K_{a2} = 3.8 \times 10^{-7}$ M^{-1}, respectively ($pK_{a1} = 4.17$ and $pK_{a2} = 6.42$). In the case of the weak acid (TFA, see Fig. 4b), three unknown variables (K_{a1}, K_{a2}, and K_a of the treated acid) are present in the theoretical equations of $[HD^+]$ and $[H_2D^{2+}]$. Therefore, the K_{a1} and K_{a2} values deduced from modelling the experimental data with TfOH were introduced as fixed parameters in the equations (Equations (16) & (17)), and then used to reproduce the experimental normalized absorbance upon TFA addition (see Fig. 4b). The best simulation leads to $pK_a = 3.54$ for TFA that corresponds well to the reported value in DMSO [Bordwell, F. G. *Acc. Chem. Res.* **1988**, *21*, 456–463].

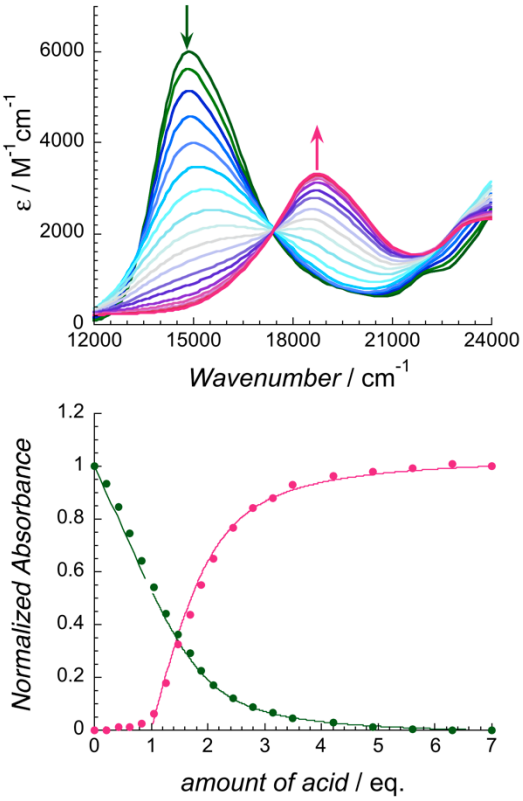

Figure S18 | UV-vis spectroscopic characterization of **[FeCo]** solution. Top, spectral evolution upon the addition of trifluoromethanesulfonic acid (TfOH) to a **[FeCo]** DMSO solution (2.68×10^{-4} M). From green to purple, the equivalence of acid is increasing with the intervals of (i) 0.21 up to 2.1 eq, (ii) 0.35 up to 3.5 eq, and (iii) 0.7 up to 7 eq. Bottom, the normalized absorbance intensities of each band; Dark green for 14800 cm^{-1} and purple for 18700 cm^{-1}. The solid lines are the results of the model described above.

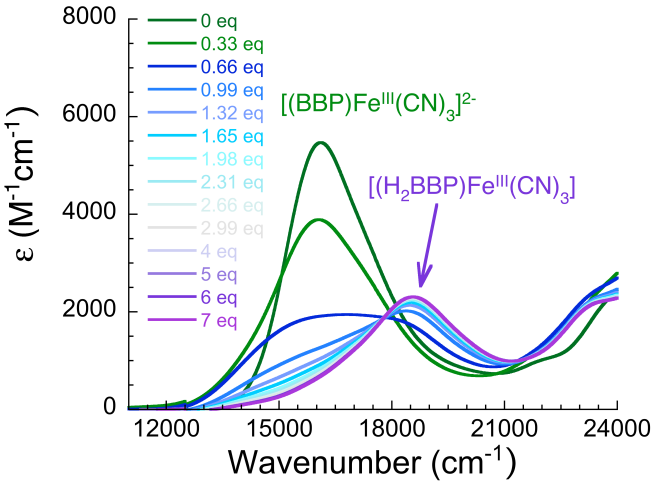

Figure S19 | Evolution of the UV-vis spectra upon TFA addition to a DMSO solution of **1** at 298 K with a concentration of 4.8 mM. The addition of TFA until 0.7 eq. does not significantly modify the UV-vis spectra around 18600 cm^{-1} suggesting, like for **[FeCo]** (Fig. 4), the absence of di-protonated analogue of **1** and thus that all added protons produce first only mono-protonated analogue. The production of the mono-protonated analogue modifies mainly the absorption spectra around 16100 cm^{-1} as observed for **[FeCo]** at 14800 cm^{-1} (Fig. 4a). Furthermore, it is worth mentioning that the di-protonated analogue of **1** is paramagnetic as proved by the NMR spectra (Fig. S11) precluding the reduction of the Fe(III) during acid addition.